

**Naval Surface Warfare Center
Carderock Division**

West Bethesda, MD 20817-5700

NSWCCD-TR-61-97/10 May 1998

**Survivability, Structures, and Materials Directorate
Technical Report**

SEM Stereo-Section Fractography Observations

by

X. Jie Zhang
Robert L. Tregoning
Ronald W. Armstrong (UMCP)
George R. Irwin (UMCP)

19980729 015



DTIC QUALITY INSPECTED 1

Approved for public release; distribution is unlimited.

**Naval Surface Warfare Center
Carderock Division**
West Bethesda, MD 20817-5700

NSWCCD-TR-61—97/10 May 1998

**Survivability, Structures, and Materials Directorate
Technical Report**

SEM Stereo-Section Fractography Observations

by

X. Jie Zhang
Robert L. Tregoning
Ronald W. Armstrong (UMCP)
George R. Irwin (UMCP)

Approved for public release; distribution is unlimited.

REPORT DOCUMENTATION PAGE

Form Approved
OMB No. 0704-0188

1. AGENCY USE ONLY (Leave blank)	2. REPORT DATE	3. REPORT TYPE AND DATES COVERED	
	September 1997	Final	
4. TITLE AND SUBTITLE			5. FUNDING NUMBERS
SEM Stereo-Section Fractography (SSF) Observations			ONR PE 62234N ONR Task Area 03460 NRC JC J6036 and B0119
6. AUTHOR(S)			8. PERFORMING ORGANIZATION REPORT NUMBER
X. Jie Zhang and Robert L. Tregoning (NSWC) Ronald W. Armstrong and George R. Irwin (UMCP)			
7. PERFORMING ORGANIZATION NAME(S) AND ADDRESS(ES)			NSWCCD-TR-61-97/10
1) Naval Surface Warfare Center, Carderock Division, W. Bethesda, MD 20817-5700 2) University of Maryland, College Park, MD 20742			
9. SPONSORING/MONITORING AGENCY NAME(S) AND ADDRESS(ES)			10. SPONSORING/MONITORING AGENCY REPORT NUMBER
1) Office of Naval Research, Code 332, Arlington, VA 22217, program element 62234N, task area 03460 2) Nuclear Regulatory Commission, HSTP, Washington DC 20555, job codes J6036 and B0119			
11. SUPPLEMENTARY NOTE			
12a. DISTRIBUTION/AVAILABILITY STATEMENT			12b. DISTRIBUTION CODE
Approved for public release; distribution is unlimited.			
13. ABSTRACT (Maximum 200 words) <p>Cleavage initiation in engineering materials is governed by local microstructural inhomogeneities. These features are often the principal reason for the large scatter evident in fracture toughness measurements which, in extreme cases, can mask the fundamental relationship between cracking resistance and global material properties. The SEM stereo-section fractography (SSF) technique can be used to carefully evaluate these local inhomogeneities through simultaneous observation of both the fracture surface and the underlying microstructure. By sectioning the fracture surface close to the cleavage initiation site (within 10 µm), and perpendicular to both the fracture surface and the precrack front, a direct correspondence between initiation and the local microstructure can be established. Information obtained from this technique can provide quantitative input about important, local microstructural features which can then be used to calibrate or create realistic micromechanical models. A compendium of SSF results is presented herein for cleavage cracking in disparate materials (A533B steel plates, MIL-70S multi-pass weldments, and Ti6Al4V forgings), under various testing conditions. In each case, the SSF technique was able to unambiguously identify the dominant, local features which triggered cleavage initiation.</p>			
14. SUBJECT TERMS			15. NUMBER OF PAGES 24
Fractography, Cleavage initiation, Fracture toughness, Steel, Titanium, Weldment			16. PRICE CODE
17. SECURITY CLASSIFICATION OF REPORT Unclassified	18. SECURITY CLASSIFICATION OF THIS PAGE Unclassified	19. SECURITY CLASSIFICATION OF ABSTRACT Unclassified	20. LIMITATION OF ABSTRACT Same as Report

Contents

Abstract	vi
Administrative Information	vi
Introduction	1
Cleavage Initiation in A533B Steel: Effect of Carbide Banding	2
Cleavage Initiation in A533B Steel Biaxial Testing: Effect of Microstructural Variability ..	3
Specimen BB10	4
Specimen BB07	7
Cleavage Initiation in Mil-70s Multi-Pass Weldments	7
Microstructure Characterization	8
SSF Results	10
Cleavage Initiation in Ti6Al4V Environmental Fatigue Testing: Effect of Texture	13
Summary	16
References	17
Initial Distribution.....	19

Figures

1. Typical transverse section created by the SSF technique	1
2. SEM fractographs showing a substantial difference in ductile extension between specimens (a) C21U2 and (b) C21B5	3
3. Optical micrographs of transverses section showing the locations of the MCIR and the fatigue precrack tip for specimens (a) C21U2 and (b) C21B5	3
4a. An SEM micrograph of the banding structure in specimen BB10	5
4b. An SEM micrograph of equiaxed ferrite grain structure of the dark band in 4a	5
4c. An SEM micrograph of tempered martensitic or/and tempered bainitic structure of the light band in 4a	5
4d. An optical micrograph showing a significant difference in Vickers indentation size between the two microstructures	5
5a. A conventional SEM fractograph of specimen BB10 showing the location of the MCIR	6

5b. A conventional SEM fractograph of specimen BB10 after sectioning	6
5c. An SSF fractograph: fracture surface and microstructure of the transverse section around the CIS illustrated simultaneously	6
6. An optical micrograph of the transverse section of specimen BB07	7
7. A simplified sketch of the microstructural zones present in a multi-pass weldment	8
8a. The weld bead structure of specimen GXK 62	9
8b. The microstructure surrounding the fusion line of one weld bead, line A-A in 8a	9
9a. A low magnification conventional SEM fractograph of specimen GXK 62	11
9b. An enlargement of the MCIR in 9a	11
9c. Fracture surface and microstructure of the CIR region: tilted 45° about the section axis	11
10. An optical micrograph of specimen GXK 62 showing the location of the fatigue precrack tip and the CIS with respect to the welding bead structure	12
11. An optical micrograph of specimen GXK 59 showing the location of the fatigue precrack tip and the CIS with respect to the welding bead structure	12
12. Fatigue crack growth rate behavior of Ti6Al4V forging: specimen SIR-26A	13
13a. A conventional SEM fractograph of specimen SIP-26A showing three distinguishable features	13
13b. An enlargement of the boxed area in 13a	14
14a. An optical micrograph of the transverse section through the feature III region shown in 13a	15
14b. An enlargement of the boxed area in Figure 14a showing the long vertical secondary crack	15
14c. An SEM micrograph of the second SSF section along line A-A in 14b	15

14d. Enlargement of the boxed area in Figure 14c: a good correlation between etched microstructure and secondary cracking fracture planes is apparent 16

Abstract

Cleavage initiation in engineering materials is governed by local microstructural inhomogeneities. These features are often the principal reason for the large scatter evident in fracture toughness measurements which, in extreme cases, can mask the fundamental relationship between cracking resistance and global material properties. The SEM stereo-section fractography (SSF)¹ technique can be used to carefully evaluate these local inhomogeneities through simultaneous observation of both the fracture surface and the underlying microstructure. By sectioning the fracture surface close to the cleavage initiation site (within 10 μm), and perpendicular to both the fracture surface and the precrack front, a direct correspondence between initiation and the local microstructure can be established. Information obtained from this technique can provide quantitative input about important, local microstructural features which can then be used to calibrate or create realistic micromechanical models. A compendium of SSF results is presented herein for cleavage cracking in disparate materials (A533B steel plates, MIL-70S multi-pass weldments, and Ti6Al4V forgings), under various testing conditions. In each case, the SSF technique was able to unambiguously identify the dominant, local features which triggered cleavage initiation.

Administrative Information

This work was performed by the Fatigue and Fracture Branch of the Naval Surface Warfare Center as part of the "Optimized Weld Joint Performance" subtask sponsored by the Office of Naval Research 6.2 program, PE 62234N, Task Area R3460, using work unit plans 96-1-6140-564 and 97-1-6140-732. The CDNSWC 6.2 program manager was Dr. Bill Messick (NSWCCD 0115). The work described herein was supervised by Mr. Thomas Montemarano, Head, Fatigue and Fracture Branch, NSWCCD 614.

Introduction

When studying the cleavage fracture behavior of structural alloys, it is of utmost importance to not only identify the cleavage initiation site(s), but also the underlying microstructure. This information can then be used with knowledge of the testing conditions to determine reasons for scatter within the ductile-to-brittle transition regime. More importantly, once the microstructure has been identified, possible changes can be explored in an effort to improve the material's cracking resistance. However, relating initiation to local microstructural features is practically challenging due to both the small size-scale of typical cleavage initiation sites --- 10 μm or less --- and the difficulty in viewing the microstructure and fracture surface in tandem. Good edge retention must be maintained and the microstructure must be closely juxtaposed to the initiation site to ensure its authenticity. The SEM stereo-section fractography (SSF) technique¹ has been developed to overcome these obstacles and allow the fracture surface and the surrounding microstructure to be observed simultaneously.

Figure 1 illustrates the basic objective of this technique which is to prepare a transverse section adjacent to the main cleavage initiation site (MCIS). A transverse section is first cut and polished near the MCIS while the fracture surface is protected with an acetone-soluble polymeric coating.¹ The coating is then dissolved and the proximity of the transverse section to the cleavage site is ascertained. The fracture surface is coated again and the transverse surface is ground and polished to move the section closer to the MCIS. The protective coating is again removed for examination and the process is carefully repeated. In this manner, the final section can be located within a few microns of the MCIS. A final light polish and etch is then applied to reveal the microstructure and the fracture surface features and transverse-section microstructure are then ready to be examined simultaneously.

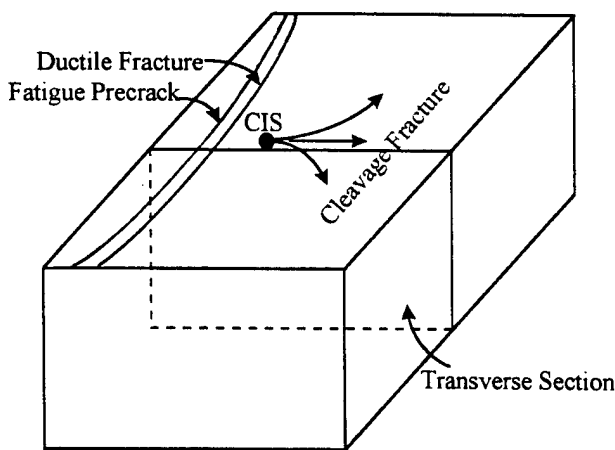


Figure 1: Typical transverse section created by the SSF technique.

In this report, SSF results are presented for three different materials (an A533B steel plate, a MIL-70S multi-pass weldment, and a Ti6Al4V forging) which were tested under different loading conditions (quasi-static bend, biaxial tension, and cyclic loading). The results demonstrate that this technique is useful for establishing a direct correspondence between the fracture surface morphology and the underlying microstructure. In all these alloys, microstructural inhomogeneities and texture were found to consistently trigger cleavage initiation. These local features also provided a clear explanation of the inherent scatter within bulk fracture toughness measurements for these alloys. Although the feature which triggered cleavage varied among the materials, a single dominant embrittled region was consistently apparent for a given material.

Cleavage Initiation in A533B Steel: Effect of Carbide Banding

Carbide banding is one prevalent microstructural non-uniformity in heavy section plates of quenched and tempered A533B steel. The banding is relatively coarse (on the order of tens of microns) and is due to segregation during the solidification process. Significant carbon content and hardness differences between the high and low carbon bands have been found.^{2,3} These differences imply that the high carbon bands are stronger and more brittle and also that the local mechanical properties are not uniform. Therefore, it should be expected that the location of fatigue precrack tip with respect to the banding substructure will be crucial to the overall fracture performance. Previously, Irwin, Armstrong, Zhang and et al. have shown that cleavage initiation in this type of steel is associated with high density carbide particle clusters within the carbide-rich band. It has also been demonstrated that this non-uniform structure is one of the primary sources of scatter within the fracture toughness measurements.^{1,3,4,5}

A group of nine $\frac{1}{2}$ T SENB specimens ($B= 25.4$ mm) of A533B steel were tested at -6.7°C and the J-integral values at cleavage (J_c) exhibited wide scatter.⁶ The lowest J_c was 61 m-kN/m^2 (348 in-lbs/in^2) for specimen C21U2 while the highest J_c was 306 m-kN/m^2 (1750 in-lbs/in^2) for specimen C21B5. Low magnification SEM fractographs of the two specimens (Figures 2a-2b) illustrate a significant difference in ductile fracture width between the two specimens which reflects these J_c differences. The inlaid box in each figure identifies the main cleavage initiation region (MCIR). A transverse section (as in Figure 1) was created a few microns away from the cleavage initiation site (CIS) in each specimen. The section was then etched and imaged optically (Figures 3a- 3b) to reveal the adjacent microstructure. The fatigue precrack tip, ductile zone width, and cleavage initiation site are indicated for each specimen in these figures. Their precise locations have been maintained here by tilting the specimen to reveal both the fracture surface and microstructure, identifying distinguishing features on each surface, and then slowly tilting the specimen until the transverse section is normal to the imaging beam. It is then clearly evident that the narrower ductile fracture zone and subsequent rapid onset of cleavage observed in specimen C21U2 is associated with the relatively brittle, dark carbide band. Conversely, the wider ductile fracture zone and higher toughness of specimen C21B5 is

associated with a relatively ductile, lower carbon region. The underlying microstructure explains the substantial spread of J_c in these specimens, but it even more clearly demonstrates Irwin's conjecture that cleavage initiation is a local event which is sensitive to microstructural variation within the material.*

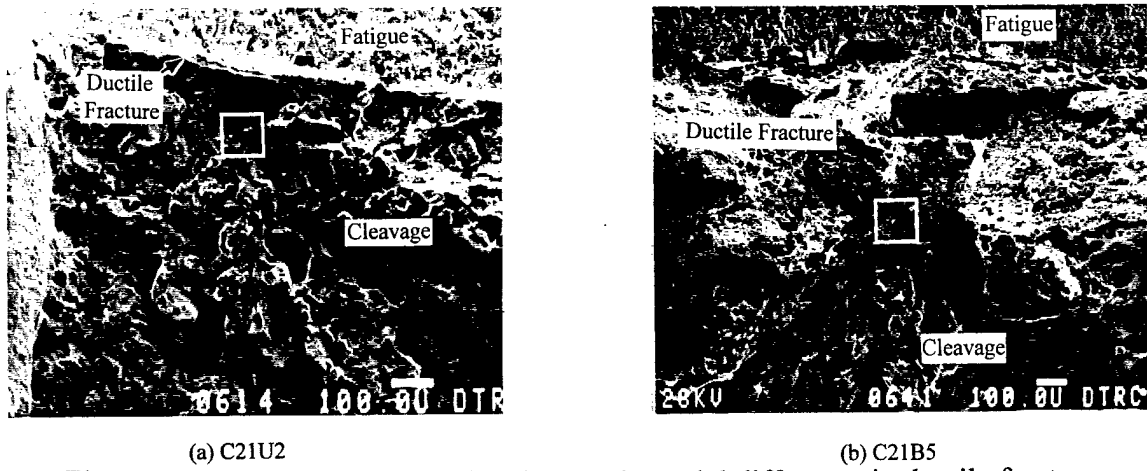


Figure 2: SEM fractographs showing a substantial difference in ductile fracture extension between specimens (a) C21U2 and (b) C21B5.

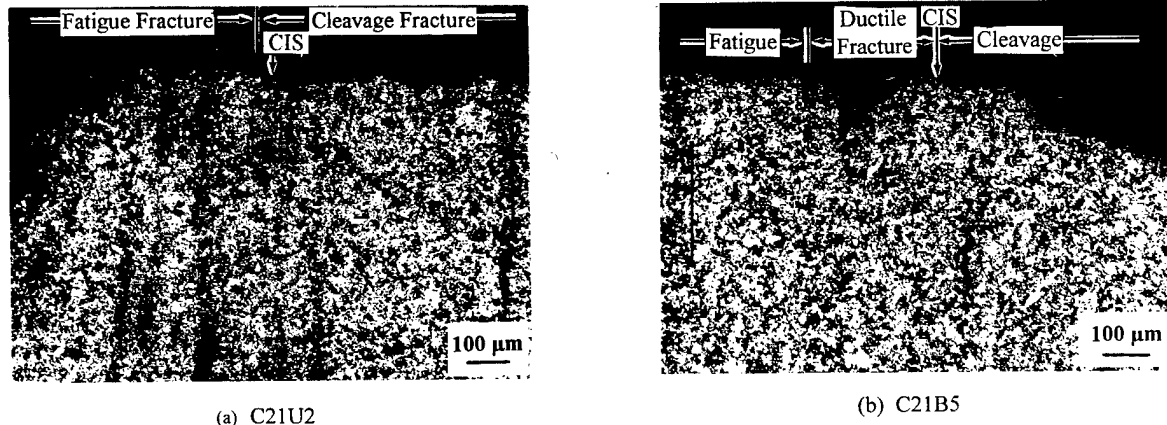


Figure 3: Optical micrographs of transverse sections showing the locations of the MCIR and the fatigue precrack tip for specimens (a) C21U2 and (b) C21B5.

Cleavage Initiation in A533B Steel Biaxial Testing: Effect of Microstructural Variability

It is well known that low crack-tip constraint contributes to both an increase in scatter and in median J_c measurements by reducing the hydrostatic stress component ahead of the crack tip.^{7,8}

* Irwin, G.R. and X. J. Zhang, Private communication, March 1996.

Traditional uniaxial testing methodology has evolved to ensure high crack-tip constraint, so that both a lower-bound material toughness is measured and the scatter is reduced. A new cruciform specimen, biaxial testing methodology has been developed⁹ by extending this rationale to determine if increased out-of-plane constraint in structurally relevant, shallow flawed specimens leads to cleavage initiation toughness values which are lower than measured in uniaxial testing. The testing apparatus allows the normal-to-transverse stress ratio within the test section to be varied from 1:0 to 1:1 to simulate from uniaxial to maximum out-of-plane constraint.

Early results, however, exhibited substantial scatter in K_{JC} measurements even in the 1:1 biaxial tests. The K_{JC} was 113 MPa \sqrt{m} (103 ksi \sqrt{in}) for specimen BB10, while the K_{JC} was 219 MPa \sqrt{m} (199 ksi \sqrt{in}) for specimen BB07.⁹ Such discrepancies were not expected due to the high crack-tip constraint, and microstructural reasons for the scatter were sought using the SSF technique.

Specimen BB10

Metallurgical analysis revealed that specimen BB10 had a pronounced banding structure. Further, substantial microhardness variations were found between the banded regions within the material. This banded microstructure is evident in a low-magnitude SEM micrograph (Figure 4a) of the transverse surface which is approximately 5 μm from the MCIS. This structure is similar to the different heat of this steel discussed earlier (Figure 3a, b).

Higher magnification SEM micrographs (Figures 4b, 4c) illustrate the microstructure typical of these bands. The dark bands in Figure 4a consist of equiaxed ferrite grains (Figure 4b) which have no carbide precipitates within the grains and relatively few carbide particles scattered along the grain boundaries. The light bands in Figure 4a contain tempered martensite and/or tempered bainite and are characterized by dense carbide particles aligned along preferred orientations within the grains (Figure 4c). An optical image of adjacent bands is illustrated in Figure 4d. Imaging differences between the SEM and light microscope cause the equiaxed ferritic bands to appear darker than the transformed bands in the SEM and lighter optically. Hardness measurements within each region reveal that the equiaxed ferritic band --- the lighter region in Figure 4d --- has lower hardness (164 VHN) while the transformed band is 30% harder (210 VHN). It should therefore be expected that the transformed banding structure is more brittle than the equiaxed ferritic bands and should act as preferential sites for cleavage initiation.

The location of the fatigue precrack tip and cleavage initiation sites with respect to the banding structure for this specimen were determined using the SSF technique in the usual manner. A low-magnification SEM fractographic view (Figure 5a) was first used to identify the MCIR of specimen BB10, and then the transverse section was prepared. The left-hand portion of the fracture surface after sectioning (Figure 5b) illustrates that the section plane is within 5 μm from the MCIS. After etching and tilting the specimen 30° (Figure 5c), the banded microstructure at the MCIS is clearly visible. Slowly rotating the specimen while identifying

visual cues allows the transverse section to be fully viewed at lower magnification (Figure 4a) while maintaining the position of critical fracture surface features. Here the extent of the banded region and its juxtaposition to the fatigue precrack tip is obvious and unequivocally shows that the brittle, transformed microstructure triggered cleavage and the low measured toughness ($113 \text{ MPa}\sqrt{\text{m}}$) results from the fatigue precrack's proximity to this brittle banded region.

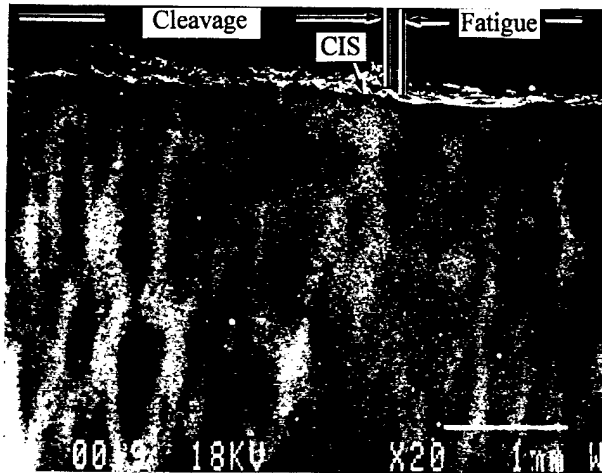


Figure 4a: An SEM micrograph of the banding structure in specimen BB10.

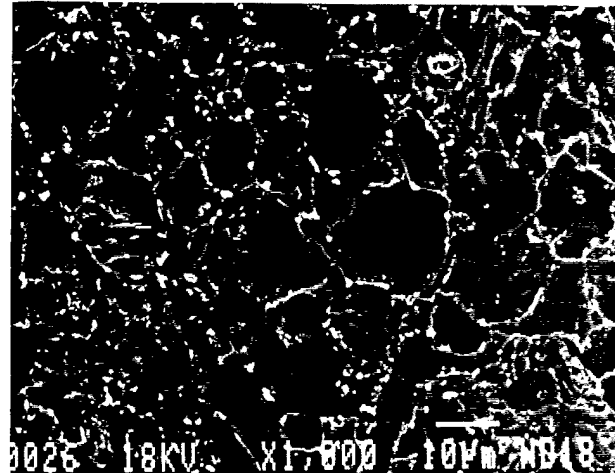


Figure 4b: An SEM micrograph of equiaxed ferrite grain structure of the dark band in 4a.

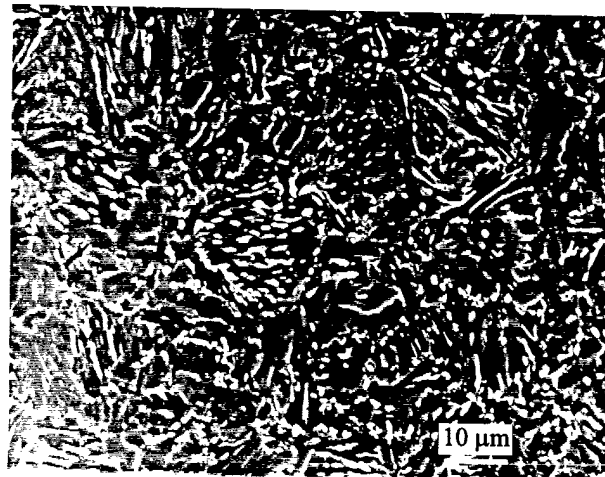


Figure 4c: An SEM micrograph of tempered martensitic or/and tempered bainitic structure of the light band in 4a.

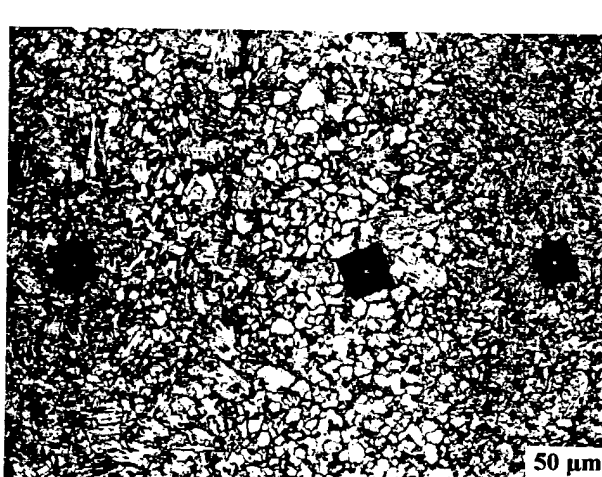


Figure 4d: An optical micrograph showing a significant difference in Vickers indentation size between the two microstructures.

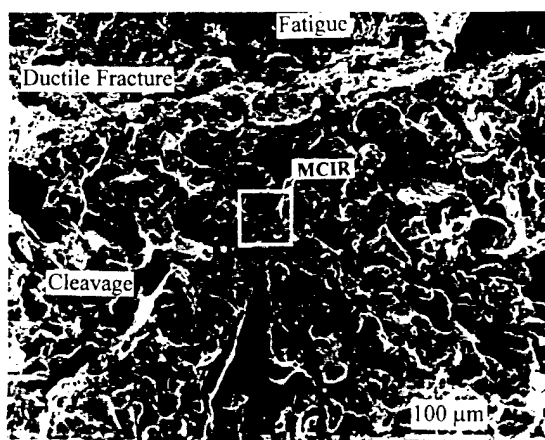


Figure 5a: A conventional SEM fractograph of specimen BB10 showing the location of the MCIR.

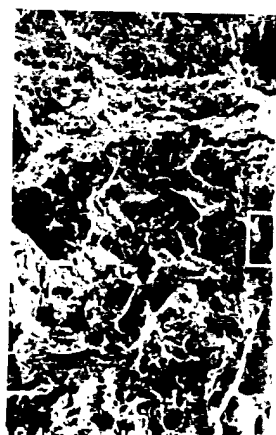


Figure 5b: A conventional SEM fractograph of specimen BB10 after sectioning.



Figure 5c: An SSF fractograph: fracture surface and microstructure of the transverse section around the CIS illustrated simultaneously.

Specimen BB07

The microstructure of this specimen is relatively uniform. Carbide particles are randomly distributed within the ferrite grains and there are slight variations in grain size, shape, and carbide particle density within the matrix (Figure 6). However, no banding is apparent here and the microstructure is substantially different than in specimen BB10 (Figure 5a). Microhardness measurements for this specimen exhibited a negligible variation as a function of location, and the average value was 183 VHN which is substantially lower than the brittle, transformed bands present in BB10. This easily explains why the ductile tearing region was so large in this specimen and consequently why the measured toughness was so much higher than for BB10.

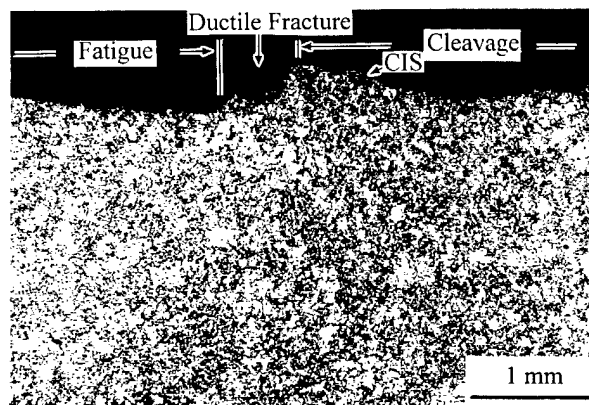


Figure 6: An optical micrograph of the transverse section of specimen BB07.

These microstructural observations indicate that specimens from different locations within the same heavy-section steel plate can have dramatically different microstructures due to the solidification process and heat treatment history. Further, this variation governs the fracture performance and once again illustrates the fundamental interrelationship between cleavage initiation and the local microstructural features. The inhomogeneities within the local microstructure therefore invariably lead to scatter in fracture toughness measurements which cannot be eliminated, regardless of the severity of the local, crack-tip constraint. It should be possible to use these differences to provide a more rigorous, quantitative index of the material's toughness in much the same way that global chemistry and microstructural effects have historically been used. Further, these results indicate that the influence of the local microstructure and microstructural non-uniformity on cleavage should be rigorously incorporated into any cleavage-initiation models of steels.

Cleavage Initiation in Mil-70s Multi-Pass Weldments

Extensive fractographic observations were performed on several mismatched 1T SE(B) weldment specimens. The specimens were constructed from HY-80 base plate and MIL-70S

weld wire using an unsymmetric double-V joint. The crack tip was located within the center of weld.¹⁰ Five specimens were examined using the SSF technique to evaluate the effect of welding zone microstructure on cleavage initiation. This technique was especially helpful in this study due to the extent of the local, small-scale variability inherent in multi-pass weld microstructure. Once again, it was determined that cleavage initiation could be traced to a single region; in this case the region was a narrow band of material surrounding the fusion line.

Microstructure Characterization

A simplified sketch of the microstructural zones present in a multi-pass weldment (Figure 7) illustrates the inhomogeneity associated with a single weld bead pass. Each welding pass produces: (a) a coarse columnar zone (CCZ) bounded by a visible fusion line (solid line in Figure 7) which exhibits the structural characteristics of a casting; (b) a fully transformed heat-affected zone (HAZ) in the base metal or previous weld beads, which can be further divided into a coarse grain (CGHAZ) and a fine grain (FGHAZ) region; (c) a partially transformed heat-affected zone (PTHAZ) next to the FGHAZ, which is heated to temperatures between A_{c1} and A_{c3} ; and (d) a tempered HAZ zone (THAZ) where the temperature has remained lower than A_{c1} . The microconstituents formed in each zone is a function of the weld filler chemistry and the welding parameters. Furthermore, in a multi-pass weld, a portion of the previous coarse columnar zone is reheated by the HAZ of subsequent passes (dashed line in Figure 7). These portions of the prior bead's coarse columnar region then essentially become form part of the HAZ of the succeeding bead. The central portion of the bead retains its original, untempered structure (CCZ in Figure 7).

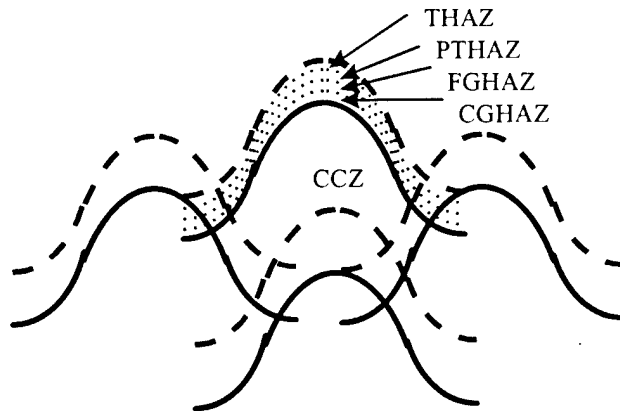


Figure 7: A simplified sketch of microstructural zones present in a multipath weldment.

Figure 8a illustrates the weld bead microstructure of specimen GXK 62. The microstructure surrounding the fusion line of one bead (A-A in Figure 8a) has been magnified in Figure 8b. In this picture, the FGHAZ, CGHAZ, fusion line, and the edge of the CCZ are evident. It is important to note the similarity between the CGHAZ and the edge of the CCZ adjacent to the fusion line: both contain allotriomorphic ferrite along the prior austenite grain

boundaries, Widmanstatten side plates, acicular ferrite, and carbide particle clusters. The features of these bands compared to the remainder of the weld bead microstructure suggest that this narrow region surrounding the fusion zone is the most brittle. Therefore, the CGHAZ and edge of the CCZ should serve as the preferential cleavage initiation region for this group of weldments.



Figure 8a: The weld bead structure of specimen GXK 62.

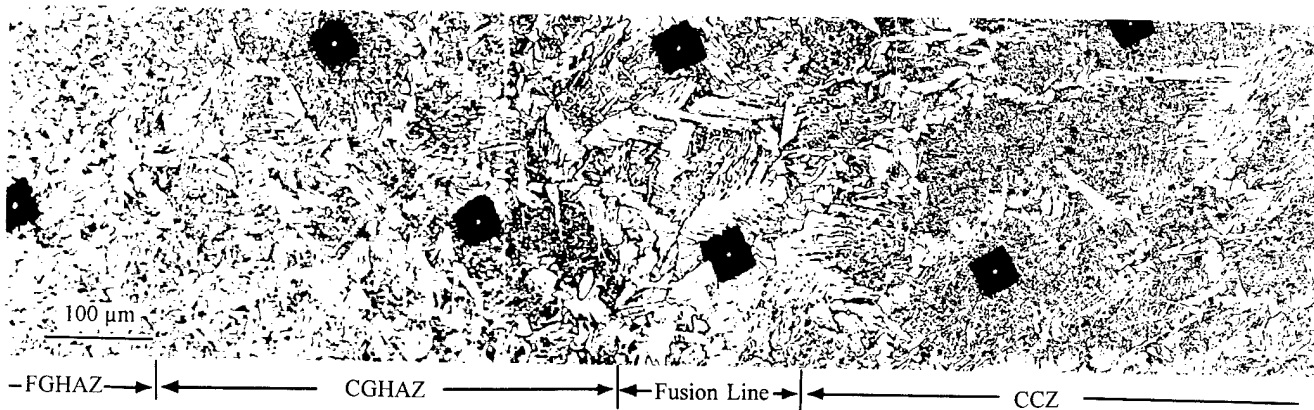


Figure 8b: The microstructure surrounding the fusion line of one weld bead; line A-A in 8a.

In single-pass weldments, the CGHAZ in the base metal is typically the most brittle weld zone region due to the formation of large prior austenite grains and fast cooling transformation products (such as allotriomorphic ferrite, Widmanstatten side plates, acicular ferrite, bainite, and martensite). The finding that both the edge of the CCZ and CGHAZ have similarly embrittled characteristics in this multi-pass weldment is due to the increased cooling rate possible near the

fusion line from previously deposited weld beads. In addition, the edge of the CCZ retains the inherently weak as-deposited microstructure and may be even further embrittled due to segregation. It is therefore likely that the edge of the CCZ may be even more embrittled than even the reaustenitized CGHAZ.

SSF Results

The SSF results indicated that the MCIS in four of the five sectioned GXK specimens was located at the edge of the CCZ, adjacent to the fusion line. Specimen GXK 62 is typical of these specimens. The unsectioned fracture surface of this specimen (Figure 9a) clearly indicates the dominant CIS. The focal point of the site (within the white box in Figure 9a) is enlarged in Figure 9b and the cleavage initiation site has been identified by the black arrow. A transverse section was then prepared approximately 10 μm from the cleavage initiation site. Figure 9c shows the fracture surface and transverse section simultaneously after tilting the specimen 45° about the sectioning axis. In the figure, the small triangular cleavage facet near the cleavage initiation site (indicated by black arrow) was used to identify the location of the MCIS as the section was rotated to view solely the transverse microstructure surrounding the CIS and fatigue precrack (Figure 10). It is evident in Figures 9c and 10 that cleavage initiation was associated with long ferrite plates at the edge of the CCZ, adjacent to the fusion line. Further, it is evident that (1) the tip of the fatigue pre-crack was located in the middle of the CCZ; (2) ductile crack growth proceeded through the CCZ for approximately 1 mm without triggering cleavage cracking; and (3) cleavage was triggered only when the edge of the CC microstructure was sampled by the crack tip. As mentioned earlier, four of the five GXK specimens examined also exhibited cleavage initiation only within the CCZ, near the edge of the fusion line.

The only specimen analyzed that did not cleave within this region was GXK 59. The cleavage site was identified, and the transverse section was prepared as before. Once again, the transverse section was located within 10 μm from the CIS. The final etched section is shown in Figure 11. The fatigue crack tip in this specimen was located within the FGHAZ of this weld pass. The crack initiated as a stable, ductile crack and propagated through the FGHAZ, toward the fusion line. Only when the crack reached the CGHAZ, did cleavage initiation occur. Therefore, although the edge of the CCZ was not the triggering site in this specimen, the other susceptible microstructural site was responsible.

The SSF results of this MIL-70S weldment system establish that the microstructure surrounding the narrow fusion line governs cleavage initiation. Therefore, the distance between the fatigue crack tip and the fusion line region in the direction of crack propagation determines the amount of ductile tearing. The measured toughness results reinforce this observation: The lowest J_c value from this subset of specimens was 37 m-kN/m² (210 in-lbs/in²) and corresponded to a specimen where the fatigue precrack was within 75 μm from the fusion line. Conversely, the highest J_c measured was 382 m-kN/m² (2180 in-lbs/in²) and represents the specimen where the fatigue precrack tip was furthest from the fusion line.

It appears that it is possible to eliminate virtually all the measured scatter in J_c in this (and similar) weldment system with knowledge of the material's J-R curve and the distance from the fatigue precrack tip to the fusion line. It is also clear that any improvement in the fracture toughness of this weld can only be possible if the toughness of the fusion line microstructure is increased, such as by reaustenization of the underlying beads. Some initial efforts in this area have been made by Albery and Jones,¹¹ and Reed.¹²

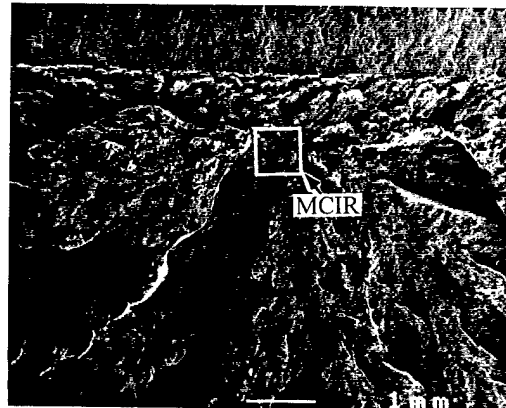


Figure 9a: A low magnification conventional SEM fractograph of specimen GXK 62.



Figure 9b: An enlargement of the MCIR in 9a.



Figure 9c: Fracture surface and microstructure of the CIS region: tilted 45° about the section axis.

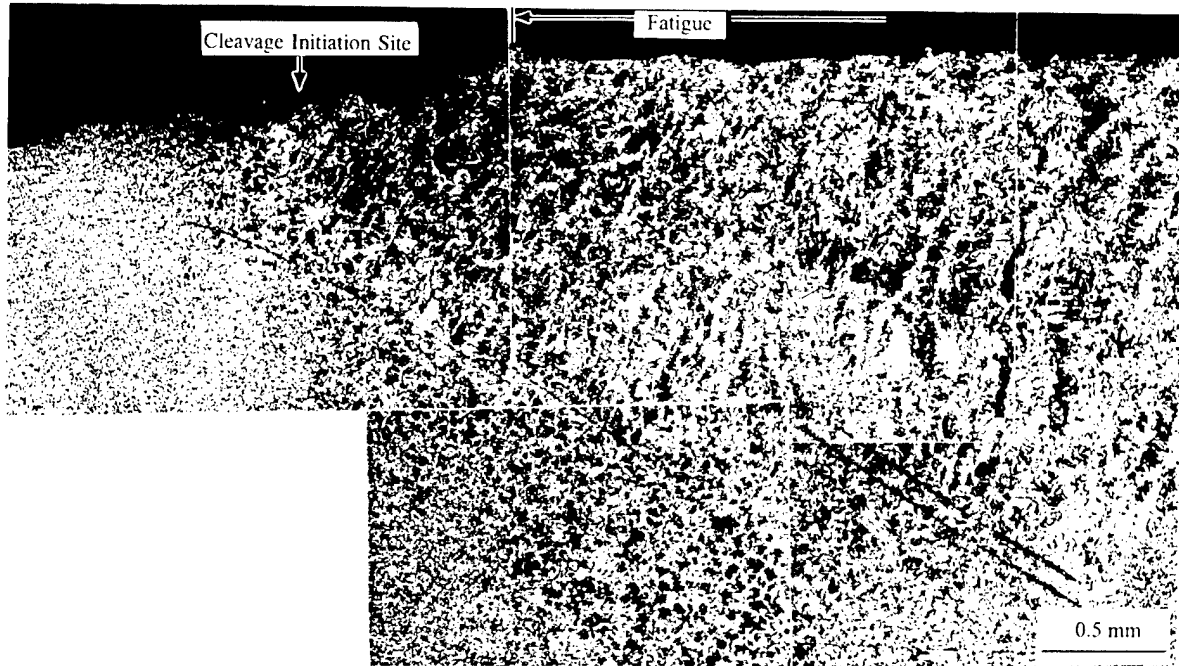


Figure 10: An optical micrograph of specimen GXK 62 showing the location of the fatigue precrack tip and the CIS with respect to the welding bead structure.

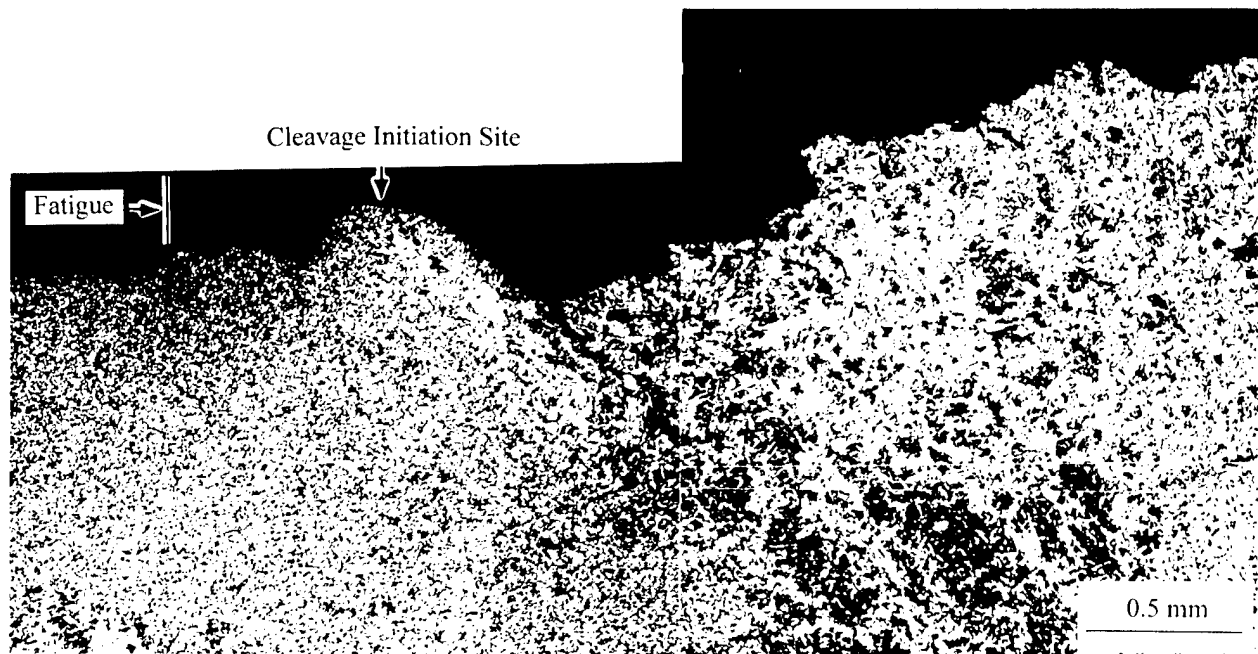


Figure 11: An optical micrograph of specimen GXK 59 showing the location of the fatigue precrack tip and the CIS with respect to the welding bead structure.

Cleavage Initiation in Ti6Al4V Environmental Fatigue Testing: Effect of Texture

The SSF technique was also applied to study the cracking behavior of a Ti6Al-4V forging. This material was tested in 3.5% NaCl at room temperature under constant amplitude, $R=0.1$ loading. The fatigue crack growth rate (FCGR) behavior was highly nonuniform and exhibited sporadic crack growth acceleration and deceleration, especially between $10 \text{ MPa}\sqrt{\text{m}} < \Delta K < 20 \text{ MPa}\sqrt{\text{m}}$ (Figure 12). Fractographic observation revealed three distinct features on the fatigue surface which contribute to this behavior (Figure 13a): (I) coplanar faceted regions; (II) brittle, randomly-oriented faceted regions; and (III) peculiar transverse regions featuring crystallographic facets and out-of-plane steps or jogs. An enlargement of one of these areas (Figure 13b) illustrates one of the peculiar surface feature III regions.

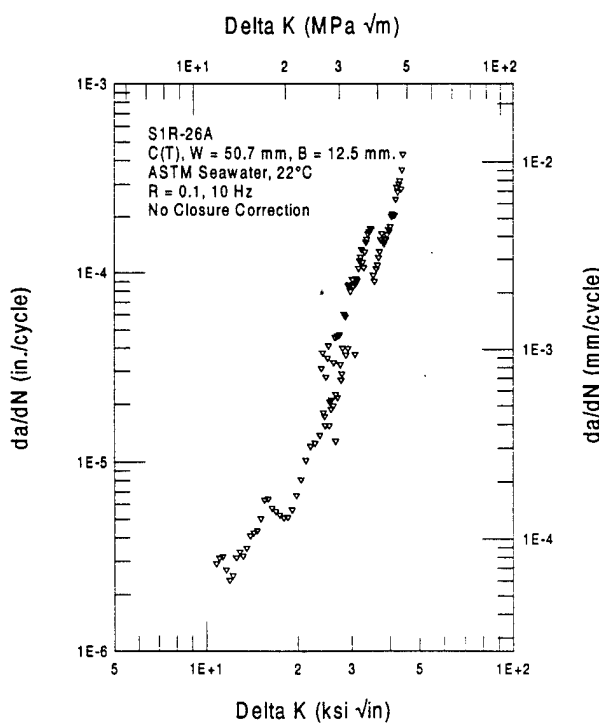


Figure 12

Figure 12: Fatigue crack growth rate behavior of Ti6Al4V forging: specimen SIR-26A.

Figure 13a: A conventional SEM fractograph of specimen SIP-26A showing three distinguishable features.



Figure 13a



Figure 13b. An enlargement of the boxed area in Figure 13a.

The SSF technique was again utilized to examine the usual transverse section (Figure 1) through a feature III region. These sections are revealed in Figures 14a and 14b and the acuity of these ledges becomes apparent; each is on the order of 100 - 200 μm out of the fracture plane. Closer examination of one of the troughs reveals extensive out-of-plane cracking that follows elongated α grains. A second SSF section was made perpendicular to the section in Figure 14b (section A-A) near the trough illustrated in this figure. The transverse cracking path is now clearly shown to propagate along elongated α grains with a preferred orientation (Figure 14c). An enlargement of the trough (boxed area in Figure 14c) illustrates the coplanar nature of this cracking as shown in Figure 14d. The top-most plane is evident in the bottom portion of Figure 14d and is actually the polished and etched microstructure of section A-A (Figure 14b). The layers below this plane are the fracture surfaces of the secondary cracks that appear to the left of section A-A (Figure 14b). The correspondence between the crack surfaces and the microstructure is striking and indicates the crystallographic nature of this cracking, the relative weakness of this orientation, and the strong texture within this region.

These pictures elucidate the correspondence between the secondary cracking path and the orientation of the elongated α grains. The α grain orientation texture was produced during the solidification process and was not eliminated by subsequent heat treatment. The crystallographic appearance of this cracking implies that a cleavage-type mechanism may govern this phenomenon. This out-of-plane cracking is not desirable because of both its brittle nature and the fact that it implies this microstructural orientation is much weaker than in the normal plane within these regions. The texture can be eliminated through proper solution heat treatments to form either randomly oriented, equiaxed α grains mixed with $(\alpha + \beta)$ constituents, or a fully transformed structure. A more homogeneous, isotropic, and stronger fracture performance should then be achievable.

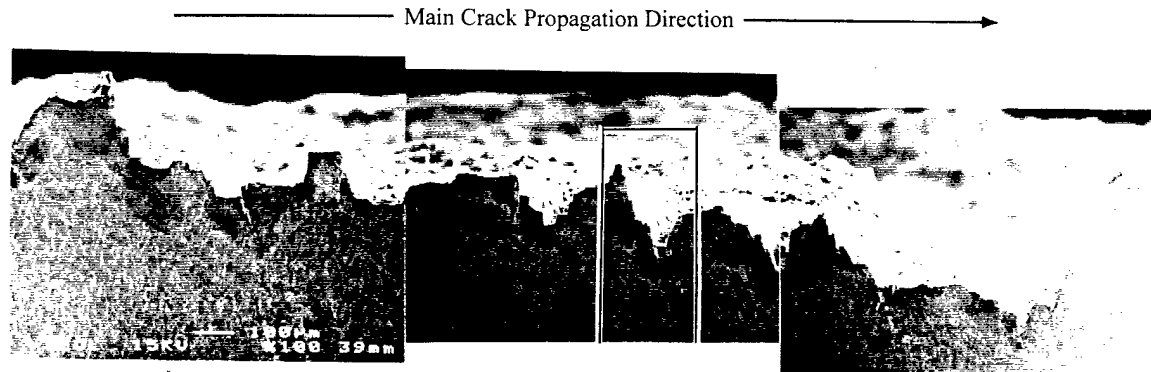


Figure 14a: An optical micrograph of the transverse section through the feature III region shown in Figure 13a.



Figure 14b: An enlargement of the boxed area in 14a showing the long vertical secondary cracks.

Figure 14c: An SEM micrograph of the second SSF section along line A-A in 14b.



Figure 14d: Enlargement of the boxed area in Figure 14c: a good correlation between etched microstructure and secondary cracking fracture planes is apparent.

Summary

In this paper, the SSF results obtained from three different materials (a A533B plate, a MIL-70S multi-pass weldment, and a Ti 6Al4V forging) and three different types of tests (SE(B), biaxial tension, and fatigue) reinforce three primary points:

1. The stereo-section fractography technique can be used to reveal the microstructure located directly adjacent to the fracture surface feature of interest. This information is vital for establishing a direct relationship between the principal fracturing mechanism and the precipitating microstructural features.
2. Microstructural inhomogeneities governed the onset of cleavage in the materials studied herein. High carbon banded regions were identified as the triggering microstructure for the A533B plates while the microstructure surrounding the fusion line was the initiation site in MIL-70S multi-pass weldments. Ti 6Al-4V exhibited secondary, cleavage-like cracking along preferably oriented α grains within a 3.5% NaCl environment. While the specific constituency of the microstructurally brittle phase varied in all these materials, one dominant region was always found to be the underlying cause of cleavage initiation.
3. The distance between the sharp advancing crack front and the initiating microstructure is an underlying reason behind the inherent scatter in fracture toughness measurements within the ductile-to-brittle transition regime. While scatter can be minimized by increasing crack-tip constraint, the remaining measured variability is indicative of the local material inhomogeneities which exist along the cracking plane.

References

1. Zhang, X. J., R. W. Armstrong, and G. R. Irwin, "Stereo (SEM) Section Fractography of Isolated Cleavage Regions in Nuclear Vessel Steels," Metall. Trans. 20A (1989) pp.2862-2868.
2. Ogawa, K., X. J. Zhang, T. Kobayashi, R. W. Armstrong, and G. R. Irwin, "Microstructural Aspects of the Fracture Toughness Cleavage-Fibrous Transition for Reactor-Grade Steel," Fracture Mechanics: Fifteenth Symposium, ASTM STP 833, R. J. Sanford, Ed., American Society for Testing and Materials, Philadelphia, 1984, pp. 393-411.
3. Zhang, X. J., "Cleavage-Fibrous Transition Behaviors of Structural Steels," Ph. D. Thesis, University of Maryland, College Park, MD, 1985.
4. Irwin, G. R., X. J. Zhang, and R. W. Armstrong, "Isolated Cleavage Regions in the Ductile Fracturing Transition of Nuclear Vessel Steels and Their Weld Metals", J. Mater. Lett.8 (1989), pp. 844-848.
5. Gudas, J. P., G. R. Irwin, X. J. Zhang, and R. W. Armstrong, "A Model for Transition Fracture of Structural Steels from Observations of Isolated Cleavage Regions," in Defect Assessment in Components - Fundamentals and Application, ESIS/EGF9, J.G. Blauel and K.H. Schwalbe, Eds., Mechanical Engineering Publications, London, 549-568, 1991.
6. Link, R. E., and J. A. Joyce, "Experimental Investigation of Fracture Toughness Scaling Models," Constraint Effects in Fracture Theory and Applications: Second Volume, ASTM STP 1244, Mark Kirk and Ad Baker, Eds., American Society for Testing and Materials, Philadelphia, 1995.
7. Sumpter , J. D. G., and A. T. Forbes, "Constraint Based Analysis of Shallow Cracks in Mild Steel," Proceedings for TWI/EWI/IS International Conference on Shallow Crack Fracture Mechanics Testing and Applications, Cambridge, UK, 1992.
8. Shih, C.F., N. P. O'Dowd, and M.T. Kirk, "A Framework for Quantifying Crack Tip Constraint," Constraint Effects in Fracture, ASTM STP 1171, American Society for Testing and Materials, Philadelphia, 1993.
9. Pennell, W. E., B. B. Bass, J. W. Bryson, T. L. Dickson, and J. G. Merkle, Martin Marietta Energy System Inc., Oak Ridge National Laboratory, "Preliminary Assessment of the Effects of Biaxial Loading on Reactor Pressure Vessel Structure-Integrity-Assessment Technology," ORNL/LTR/95-3, Oct. 1995.
10. Tregoning, R. L., "Experimental Investigation of Mismatched Weld Joint Performance," Fatigue and Fracture Mechanics: 27th Volume, ASTM STP 1296, R.S. Piascik, J.C. Newman, and N.E. Dowling, Eds., American Society for Testing and Materials, 1996.
11. Alberry , P. J., and W. K. C. Jones, "Computer Model for Prediction of Heat-Affected Zone Microstructure in Multipass Weldmens," Met. Technol., 9, 419, 1982.

12. Reed, R. C., "The Characterization and Modeling of Multipath Steel Weld Heat-Affected Zones," Ph.D. thesis, University of Cambridge, Cambridge, U. K., 1990, chap. 3.

Initial Distribution

Outside Distribution		Center Distribution	
<u>Copies</u>	<u>Agency</u>	<u>Copies</u>	<u>Code</u>
4	NAVSEA	1	0115 (Messick)
1	SEA 03M	1	60 (Wacker)
1	SEA 03M2 (Null)	1	601 (Morton)
1	SEA 03P (McCarthy)	1	603 (Cavallaro)
1	SEA 03P2 (Nichols)	1	604 (Desavage)
		1	605 (Fisch)
2	DTIC	1	606
		1	61 (Holsberg)
3	ONR	1	61s
1	1131 (Yoder)	1	62 (Eichenger)
1	1131 (Sedricks)	1	63 (Alig)
1	332 (Vasudevan)	1	64 (Fischer)
		1	65 (Beach)
4	NRL	1	66 (Riley)
1	Code 6310	1	67 (Rockwell)
1	Code 6312 (Bayles)	1	68 (Mueller)
1	Code 6314	1	611 (Palko)
1	Code 6316	1	612 (Aprigliano)
		3	613 (Ferrara)
2	NRC	1	614 (Montemarano)
1	EMMEB/DET/RES (Vassilaros)	1	614 (Czyryca)
1	EMMEB/DET/RES (Malik)	10	614 (Tregoning)
		15	614 (Zhang)
		1	614
2	UMCP (Irwin)	1	615 (Denale)
2	UMCP (Armstrong)	1	3421
		1	3422
		1	3431